Chapter 4

The ISM in the dwarf irregular galaxy Holmberg II

4.1 Introduction

In Chapter 1, we discussed how the ISM within dwarf irregular galaxies can function as a valuable testing ground for understanding the physical mechanisms governing the formation of galaxies in the early universe. These galaxies offer an environment that closely resembles conditions prevalent in the early universe, making them excellent subjects for scientific investigation. Ho II, due to its moderate inclination angle, stands out as an especially informative sample. The high-resolution observations obtained through *AstroSat* have significantly enhanced our capacity to scrutinize the ISM within this galaxy, enabling us to study the diffuse emissions. This chapter focuses exclusively on examining the interstellar dust component within Ho II. Our study of the interstellar dust within Ho II unfolds in three main sections: Firstly, we delve into exploring the correlation between diffuse UV and IR emissions originating from the galaxy. This investigation provides crucial insights into the predominant dust grains contributing to the diffuse emissions. Secondly, we engage in modeling the diffuse FUV emission originating from dust scattering using an established model. This modeling effort aims to derive the optical properties, specifically the albedo (α) and asymmetry factor (g) for the dust grains. Lastly, we probe the diffuse IR emission attributed to thermal re-emission by dust grains heated through UV/optical photons. This investigation seeks to uncover the presence of distinct dust populations characterized by different temperatures within the galaxy.

4.2 Dust in Ho II

Similar to other dwarf irregular galaxies, the distribution of dust within Ho II occurs in clumps concentrated within regions of high HI column density. This galaxy exhibits a deficiency in PAH molecules, as evident from *Spitzer* IRS observations that revealed a low PAH/continuum ratio [155]. The 8 μm emission, associated with PAH emission, is exclusively detected in areas coinciding with H II regions in Ho II [156]. The MIR spectra of such galaxies predominantly feature warm dust emission from Very Small Grains (VSG) [157]. Higher dust temperatures are noted in Ho II and other M81 dwarfs, based on high 70μm/160μm ratio. This emission extends up to 8$'$ from the center and correlates with the HI emission [155]. This contrasts with spiral galaxies, where lower average dust temperatures contribute to a peak at $\sim$ 100 μm. Additionally, Ho II lacks sufficient molecular emission detectable in the CO band [158].

While a significant portion of the UV emission in Ho II originates from the brightest star-forming regions associated with the central star-forming arc [121], the remaining areas of the galaxy, including the interiors of the HI cavities, also exhibit this emission. The HI cavities, devoid of Hα emission except at their boundaries, mainly harbor fainter FUV stars of B or A spectral types. Moreover, substantial diffuse IR emission is observed, primarily confined to star-forming regions, arising from starlight partially absorbed and re-emitted by dust. The dust-to-gas ratio, estimated at $0.2 \times 10^{-3} M_{\odot}$ [155], indicates a significantly larger gas content compared to dust within the galaxy. Previous investigations focusing on the UV–IR range primarily targeted the bright star-forming regions of Ho II. However, the availability of high-resolution UV observations from India's *AstroSat* mission now enables the mapping of diffuse UV emission within Ho II, presenting an opportunity to study its distinctive properties.

4.3 Diffuse UV - IR correlation study in Ho II

A correlation study serves as a significant statistical method indicating the connection between two quantities. As previously mentioned, when dust particles absorb stellar radiation at shorter wavelengths, like UV and optical, they undergo heating and subsequently emit radiation at longer wavelengths, specifically IR and sub-millimeter. The emission in the NIR and MIR ranges is linked to small/very small grains at high temperatures or attributed to PAH. Conversely, the FIR emission is associated with colder dust grains. Thus, conducting a correlation analysis between UV and IR wavelengths enables us to determine the abundance and

distribution of dust populations at different temperatures, contributing to the diffuse emission.

In this work, we have made use of two correlation coefficients, which are briefly described below:

- ***Spearman rank Correlation Coefficient***: Spearman's rank correlation coefficient (ρ) serves as a reliable method for examining the monotonic relationship between two quantities, rather than focusing on a linear relationship [159]. To compute this coefficient for a set of n data pairs, the observed values (X_i, Y_i) for each pair are initially transformed into dimensionless ranks x_i, y_i. These ranks assign '1' to the highest data value for each quantity, '2' to the second highest, and so forth. Subsequently, ρ is determined by the formula:

$$\rho = 1 - \frac{6\Sigma d_i^2}{n(n^2-1)},, \tag{4.1}$$

  where $d_i = x_i - y_i$ represents the difference between the ranks of corresponding observed values, and n is the number of data pairs.

  The Spearman's rank correlation coefficient lies within the range of $[-1, 1]$. A higher value of this coefficient indicates a stronger correlation between the two quantities. Specifically, a coefficient of 1 suggests a perfect association between the ranks (as one quantity increases, so does the other), while 0 implies the association to be completely independent (the quantities are unrelated). Meanwhile, a coefficient of -1 signifies a perfect negative association between the rankings (as one quantity increases, the other decreases).

- ***Pearson Correlation Coefficient***: The Pearson correlation coefficient (r) stands as a commonly used statistical measure that measures both the strength and direction of a linear connection between two continuous variables. It evaluates how effectively the relationship between these variables can be represented by a straight line.

  The Pearson coefficient is ccomputed as:

$$r = \frac{\Sigma((X_i - X_{mean})(Y_i - Y_{mean}))}{\sqrt{\Sigma((X_i - X_{mean})^2)\Sigma((Y_i - Y_{mean})^2)}},, \tag{4.2}$$

  where X_i and Y_i denote the data points corresponding to the two variables, while X_{mean} and Y_{mean} signify the mean values of these variables.

  The Pearson coefficient is confined within the range of $[-1, 1]$, where -1 signifies a complete negative linear relationship, 1 represents a perfect positive linear relationship, and 0 implies the absence of any linear relationship altogether.

- ***Probability or p-value***: After computing the correlation coefficient, it's important to evaluate the likelihood that our computation is not merely a chance outcome, known as significance testing, typically represented by a 'p-value'. This p-value serves as a measure indicating the strength of evidence against a null hypothesis (no correlation between the two variables). Ranging between 0 and 1, a high p-value (close to 1) suggests that any correlation observed could purely be due to chance, thereby leading to acceptance of the null hypothesis. Conversely, a lower p-value (close to 0) indicates that the correlation is improbable to be a chance occurrence, providing substantial evidence against the null hypothesis. Consequently, acceptance of the alternative hypothesis, suggesting a correlation between the two quantities, becomes more pertinent.

  The p-value is derived using a two-tailed Student's t-distribution. Initially, the calculated correlation coefficient transforms into a t-statistic via the formula:

$$t = \frac{r\sqrt{N-2}}{1-r^2},, \tag{4.3}$$

  where r denotes the Pearson correlation coefficient and N signifies the number of data points. Subsequently, the p-value is obtained either through a t-distribution table or statistical software.

4.3.1 Data acquisition

Regarding UV data, our analysis relies on the observations of Ho II acquired using the UVIT instrument onboard *AstroSat*, as described in Chapter 2. Specifically, we utilized UVIT data from December 2016, in the FUV filter F154W (mean $\lambda = 1541$ Å) and the NUV filter N245M (mean $\lambda = 2447$ Å), as this UVIT observation is in close proximity in time to the epochs of certain IR data considered for the correlation study.

The IR images of Ho II were acquired from two surveys: the SINGS survey [160] and the KINGFISH survey [161]. These images were sourced from the NASA/IPAC Infrared Science Archive spanning eight distinct wavelengths: 3.6 μm, 4.5 μm, 5.8 μm, 8 μm, 24 μm, 70 μm, 100 μm, and 160 μm[1]. The images at 3.6, 4.5, 5.8, and 8 μm were acquired through the IRAC instrument[2] on the *Spitzer Space Telescope*. In contrast, the images at 24, 70, and 160 μm were obtained using the MIPS instrument[3]. Furthermore, the 100 μm

[1]For accessing SINGS and KINGFISH data, visit https://irsa.ipac.caltech.edu/data/SPITZER/SINGS/galaxies/hoii/ and https://irsa.ipac.caltech.edu/data/Herschel/KINGFISH/galaxies/HoII/PACS/, respectively.

[2]For detailed information on the IRAC instrument, refer to [57].

[3]For MIPS instrument details, see [58].

image was acquired from the PACS instrument[4] aboard the *Herschel Space Observatory*. It's important to note that a constant background level had been subtracted from each of these images beforehand.

The images underwent additional refinement to correct for potential contamination from the stars. To address stellar contamination effectively, we employed a methodology detailed by [163], built on the assumption that emission at 3.6 μm predominantly represents total stellar emission. Using specific scaling factors — 0.596, 0.399, 0.232, and 0.032 — we scaled down the 3.6 μm intensities for 4.5 μm, 5.8 μm, 8 μm, and 24 μm, respectively. Subsequently, these scaled down 3.6 μm intensities were subtracted from the respective intensities in the convolved images at their corresponding wavelengths. This method effectively isolated what we refer to as 'diffuse dust emission'. To align and convolve the IR images to a common PSF, we used IRAF tools, namely *imalign* and *psfmatch* tasks.

No correction for stellar contamination was applied on the 70, 100, and 160 μm images, as the influence of stellar contamination significantly diminishes as we progress toward longer wavelengths in the IR spectrum.

4.3.2 Selection of locations

To study the diffuse emissions away from bright star-forming regions, we identified 142 locations throughout the galaxy. These locations were chosen such that there is no detected UV sources within $10''$ radius and being at least $5''$ apart from each other. Nevertheless, it's important to note that these regions might still contain undetected faint UV sources. The UV diffuse intensities for these locations were calculated as the mean of the counts within circular apertures of $5''$ radius (equivalent to $\sim$82 parsec in size). Simultaneously, we extracted IR intensities within same $5''$-radius circular apertures at these 142 selected diffuse UV locations. However, only 33 of these locations were found with non-zero intensities across all the IR wavebands considered for our study (4.5, 5.8, 24, 70, 100, and 160 μm). The details of these 33 selected locations for the correlation study, along with diffuse FUV and NUV intensities, are provided in Table 4.1. Additionally, Table 4.2 provides the calculated IR intensities for these locations, along with their corresponding errors. An interesting observation was the absence of 8 μm emission in all the locations considered, aligning with the suggested scarcity of PAH within this particular galaxy [77].

[4]Refer to [162] for specifics.

Table 4.1 Diffuse FUV, NUV intensities, and neutral hydrogen column densities N(HI) for selected 33 locations having non-zero IR intensities. The N(HI) values have been derived from the THINGS integrated HI map. The UV intensities are in units of photons cm^{-2} s^{-1} sr^{-1} $Å^{-1}$, and N(HI) values are in units of 10^{21} cm^{-2}. Magenta colour indicates locations with N(HI) $< 1\times10^{21}$ cm^{-2}

Locations	l (deg)	b (deg)	FUV intensity	NUV intensity	N(HI)
1	144.2995	32.6691	3524.02 ± 195.43	2799.29 ± 103.08	1.60 ± 0.09
2	144.2058	32.7248	521.58 ± 105.50	419.11 ± 58.81	0.08 ± 0.008
3	144.2835	32.7029	6533.34 ± 255.21	5195.95 ± 133.38	1.48 ± 0.43
4	144.2829	32.7354	1010.03 ± 125.49	555.67 ± 62.18	0.97 ± 0.05
5	144.2714	32.6746	5021.40 ± 226.59	4901.48 ± 129.93	0.98 ± 0.11
6	144.2682	32.7303	3083.16 ± 186.10	2106.87 ± 92.62	1.04 ± 0.10
7	144.2128	32.6840	3899.69 ± 203.15	2457.21 ± 98.29	0.91 ± 0.11
8	144.3110	32.7007	3952.94 ± 204.34	2608.94 ± 100.12	0.36 ± 0.07
9	144.3063	32.6755	10922.56 ± 321.58	7897.64 ± 160.87	2.05 ± 0.21
10	144.2544	32.6734	3929.44 ± 205.28	3081.45 ± 107.11	1.44 ± 0.12
11	144.3066	32.6670	2788.49 ± 177.58	1777.78 ± 86.90	0.96 ± 0.02
12	144.3100	32.6556	1505.13 ± 141.45	871.87 ± 69.63	0.40 ± 0.05
13	144.2417	32.6750	4876.30 ± 223.23	3274.28 ± 109.47	0.27 ± 0.03
14	144.2816	32.6657	3308.87 ± 190.74	2930.76 ± 104.94	1.63 ± 0.09
15	144.2885	32.7289	4060.48 ± 207.78	2142.49 ± 93.16	2.74 ± 0.14
16	144.2847	32.6633	2864.80 ± 179.26	2344.61 ± 96.10	1.53 ± 0.08
17	144.3087	32.6598	1299.51 ± 135.44	776.81 ± 67.38	0.64 ± 0.12
18	144.2642	32.7385	1382.51 ± 137.36	779.92 ± 67.28	0.65 ± 0.10
19	144.2226	32.6552	1044.90 ± 126.64	585.59 ± 63.10	1.80 ± 0.12
20	144.2661	32.7527	451.27 ± 103.50	187.88 ± 52.70	0.78 ± 0.03
21	144.3336	32.6575	842.51 ± 119.50	435.68 ± 59.22	1.19 ± 0.09
22	144.2679	32.7278	6186.94 ± 249.07	3884.05 ± 118.01	1.42 ± 0.24
23	144.2625	32.6781	6031.80 ± 246.48	4926.88 ± 130.52	1.57 ± 0.08
24	144.2465	32.6483	484.79 ± 104.94	373.81 ± 57.76	0.52 ± 0.04
25	144.2843	32.7338	1020.05 ± 125.75	571.37 ± 62.72	1.01 ± 0.04
26	144.2823	32.6637	2583.06 ± 172.47	2330.55 ± 96.08	1.54 ± 0.08
27	144.2817	32.7376	656.15 ± 111.45	437.76 ± 59.30	0.92 ± 0.06
28	144.2418	32.6507	705.38 ± 114.13	519.10 ± 61.29	0.53 ± 0.07
29	144.2930	32.7406	790.26 ± 117.64	379.86 ± 57.89	0.93 ± 0.15
30	144.2723	32.6760	6651.67 ± 256.96	5633.73 ± 138.20	1.22 ± 0.16
31	144.2476	32.6519	1314.31 ± 135.42	1100.58 ± 74.24	0.90 ± 0.13
32	144.2721	32.7334	1441.79 ± 139.82	883.12 ± 69.57	1.10 ± 0.06
33	144.2765	32.6735	6188.49 ± 249.34	4984.33 ± 131.09	1.13 ± 0.07

Table 4.2 IR intensities in selected 33 locations. See Sec. 4.3.1 for details

Location No	l (degrees)	b (degrees)	$I_{4.5\mu m}$ (MJy sr^{-1})	$I_{5.8\mu m}$ (MJy sr^{-1})	$I_{24\mu m}$ (MJy sr^{-1})	$I_{70\mu m}$ (MJy sr^{-1})	$I_{100\mu m}$ (MJy sr^{-1})	$I_{160\mu m}$ (MJy sr^{-1})
1	144.2995	32.6691	0.0062 ± 0.0041	0.0063 ± 0.0219	0.0212 ± 0.0370	1.0850 ± 0.4762	2.0711 ± 0.1891	1.3365 ± 0.6228
2	144.2058	32.7248	0.0045 ± 0.0035	0.0097 ± 0.0228	0.0335 ± 0.0476	0.3675 ± 0.3499	0.0888 ± 0.4188	0.1896 ± 0.2158
3	144.2835	32.7029	0.0131 ± 0.0072	0.0052 ± 0.0410	0.1527 ± 0.1028	4.1669 ± 0.9138	5.2371 ± 0.3456	5.3175 ± 1.1359
4	144.2829	32.7354	0.0043 ± 0.0127	0.0245 ± 0.0210	0.0739 ± 0.0915	0.7040 ± 0.2525	2.1856 ± 0.4774	0.4082 ± 0.3509
5	144.2714	32.6746	0.0052 ± 0.0061	0.0221 ± 0.0241	0.0152 ± 0.0263	1.4038 ± 0.4099	0.2419 ± 0.2397	2.3658 ± 0.3959
6	144.2682	32.7303	0.0042 ± 0.0051	0.0009 ± 0.0343	0.0536 ± 0.0373	0.8714 ± 0.4047	0.1217 ± 0.4199	1.2483 ± 0.5298
7	144.2128	32.6840	0.0089 ± 0.0114	0.0492 ± 0.0365	0.0013 ± 0.0364	0.0950 ± 0.3539	0.0938 ± 0.3735	1.1237 ± 0.1573
8	144.3110	32.7007	0.0070 ± 0.0065	0.0219 ± 0.0195	0.0382 ± 0.0332	0.0932 ± 0.1962	2.6554 ± 0.4565	0.2270 ± 0.2994
9	144.3063	32.6755	0.0049 ± 0.0080	0.0117 ± 0.0273	0.0649 ± 0.0327	1.6511 ± 0.3393	1.8380 ± 0.4956	1.5806 ± 0.2642
10	144.2544	32.6734	0.0038 ± 0.0048	0.0111 ± 0.0222	0.0287 ± 0.0242	1.0782 ± 0.4586	0.4431 ± 0.5541	1.1277 ± 0.1548
11	144.3066	32.6670	0.0029 ± 0.0055	0.0052 ± 0.0278	0.0135 ± 0.0385	0.2171 ± 0.3018	1.1570 ± 0.4715	0.8655 ± 0.6826
12	144.3100	32.6556	0.0030 ± 0.0049	0.0138 ± 0.0262	0.0061 ± 0.0289	0.0810 ± 0.2384	2.2887 ± 0.3257	0.7581 ± 0.0427
13	144.2417	32.6750	0.0115 ± 0.0522	0.0088 ± 0.0437	0.0135 ± 0.0402	0.3768 ± 0.1624	1.4094 ± 0.3236	0.5471 ± 0.5152
14	144.2816	32.6657	0.0049 ± 0.0051	0.0080 ± 0.0208	0.0202 ± 0.0351	1.2717 ± 0.2959	0.9758 ± 0.4028	1.0013 ± 0.2101
15	144.2885	32.7289	0.0011 ± 0.0036	0.0107 ± 0.0259	0.0525 ± 0.0558	2.1309 ± 0.4932	2.6377 ± 0.5618	1.5193 ± 0.7586
16	144.2847	32.6633	0.0041 ± 0.0025	0.0168 ± 0.0184	0.0008 ± 0.0293	1.4128 ± 0.1951	1.6775 ± 0.4181	1.1351 ± 0.0553
17	144.3087	32.6598	0.0009 ± 0.0036	0.0052 ± 0.0243	0.0053 ± 0.0276	0.4203 ± 0.2480	2.2430 ± 0.5503	0.2245 ± 0.2224
18	144.2642	32.7385	0.0042 ± 0.0044	0.0064 ± 0.0225	0.0137 ± 0.0344	0.3062 ± 0.1321	0.3756 ± 0.5151	0.3313 ± 0.2365
19	144.2226	32.6552	0.0088 ± 0.0097	0.0014 ± 0.0242	0.0233 ± 0.0331	0.4190 ± 0.3380	0.8689 ± 0.4349	0.6305 ± 0.2124
20	144.2661	32.7527	0.0114 ± 0.0492	0.0095 ± 0.0298	0.0435 ± 0.0449	0.6044 ± 0.1305	2.1473 ± 0.4956	0.0313 ± 0.1627
21	144.3336	32.6575	0.0026 ± 0.0051	0.0240 ± 0.0496	0.0063 ± 0.0357	0.2864 ± 0.2863	1.2062 ± 0.5060	0.0144 ± 0.1607
22	144.2679	32.7278	0.0055 ± 0.0089	0.0270 ± 0.0316	0.0799 ± 0.0432	1.7395 ± 0.6421	0.7082 ± 0.4474	1.3012 ± 0.5407
23	144.2625	32.6781	0.0054 ± 0.0029	0.0146 ± 0.0219	0.0246 ± 0.0266	1.4907 ± 0.2342	3.2091 ± 0.3913	2.4704 ± 0.4102
24	144.2465	32.6483	0.0055 ± 0.0258	0.0102 ± 0.0152	0.0194 ± 0.0414	0.2141 ± 0.4245	0.5041 ± 0.3707	0.7612 ± 0.5002
25	144.2843	32.7338	0.0019 ± 0.0173	0.0034 ± 0.0137	0.0754 ± 0.0408	0.7050 ± 0.2847	2.8483 ± 0.2218	0.1798 ± 0.3059
26	144.2823	32.6637	0.0046 ± 0.0045	0.0105 ± 0.0183	0.0116 ± 0.0282	1.3005 ± 0.2660	0.9547 ± 0.5276	0.9787 ± 0.1291
27	144.2817	32.7376	0.0020 ± 0.0011	0.0143 ± 0.0243	0.0502 ± 0.0561	0.7400 ± 0.3167	1.4890 ± 0.2596	0.9973 ± 0.3334
28	144.2418	32.6507	0.0021 ± 0.0051	0.0058 ± 0.0238	0.0062 ± 0.0381	0.3664 ± 0.4157	1.5994 ± 0.5095	0.4009 ± 0.6219
29	144.2930	32.7406	0.0032 ± 0.0052	0.0009 ± 0.0310	0.0271 ± 0.0345	0.2107 ± 0.2292	2.2268 ± 0.3958	0.6244 ± 0.0767
30	144.2723	32.6760	0.0065 ± 0.0097	0.0180 ± 0.0330	0.0151 ± 0.0347	2.3598 ± 0.5313	0.0340 ± 0.2841	3.1375 ± 0.4827
31	144.2476	32.6519	0.0070 ± 0.0548	0.0124 ± 0.0338	0.0815 ± 0.0557	1.3963 ± 0.4828	3.3328 ± 0.6623	1.6340 ± 0.5010
32	144.2721	32.7334	0.0010 ± 0.0037	0.0159 ± 0.0286	0.0264 ± 0.0390	0.9325 ± 0.3304	0.6293 ± 0.4523	1.6947 ± 0.4395
33	144.2765	32.6735	0.0061 ± 0.0040	0.0315 ± 0.0278	0.0440 ± 0.0317	2.1421 ± 0.4936	1.0896 ± 0.3669	2.8156 ± 0.5833

4.3.3 Results and Discussions

We performed correlation calculations between the UV data (at mean wavelengths of 1541 Å, for FUV and 2447 Å, for NUV) and IR intensities for six IR wavelengths. We excluded the 3.6 μm emission from the correlation study due to its assumption as stellar emission during the correction for stellar contamination (refer to Sec. 4.3.1). To establish correlations with the 4.5 μm and 5.8 μm bands, the UVIT image was convolved to achieve a common resolution of 2.5″. Additionally, the 24 μm band was convolved to a resolution of 6″ before using UV intensities from these convolved images in the correlation calculation. However, for wavelengths beyond 24 μm, the UVIT images remained unconvolved because of the poor resolution of the IR data, which, if convolved, would have resulted in nearby UV sources contaminating the aperture fluxes.

The emission at 24 μm is attributed to the warm dust emission by VSGs, close to hot, young UV emitting stars, typically found in H II regions [164]. Similarly, the 70 μm emission, which displays a close linear correlation with the 24 μm emission [165], is regarded as a significant tracer of warm dust in galaxies [155]. In our study, we have considered the 70 μm emission as an indicator of warm dust emission as it remains unaffected from the contribution of point sources [155].

For our correlation study, we considered the 33 locations showing non-zero IR intensities across all considered wavelengths, except at 8 μm. Given that most of the dust emission in Ho II tends to be associated with regions with HI column density (N(HI)) greater than 1×10^{21} cm^{-2} [155], we utilized the THINGS integrated HI map [104] to determine the HI column densities at our considered locations. This helped us divide our locations into two distinct groups: *a*) locations with HI column densities greater than 1×10^{21} cm^{-2}, comprising 17 locations; and *b*) locations with HI column densities lower than 1×10^{21} cm^{-2}, consisting of 16 locations. Details of the HI column densities for these locations can be found in Table 4.1. In Fig. 4.1, we present the FUV vs. IR intensities plot specifically for the 17 locations characterized by N(HI) $> 1 \times 10^{21}$ cm^{-2}. These plots show an overall increase in IR intensities with increase in FUV intensity. Similar plots for NUV vs. IR intensities are displayed in Fig. 4.2. Additionally, Fig. 4.3 shows the intensity plots for locations with N(HI) $< 1 \times 10^{21}$ cm^{-2}.

Such a correlated increase of IR and UV along with its inherent spread may indicate spatial variations of the dust mass in illuminated clouds and the illuminating UV intensity, as well. The spread of IR intensities might be also attributed to random variations of the mass-to-

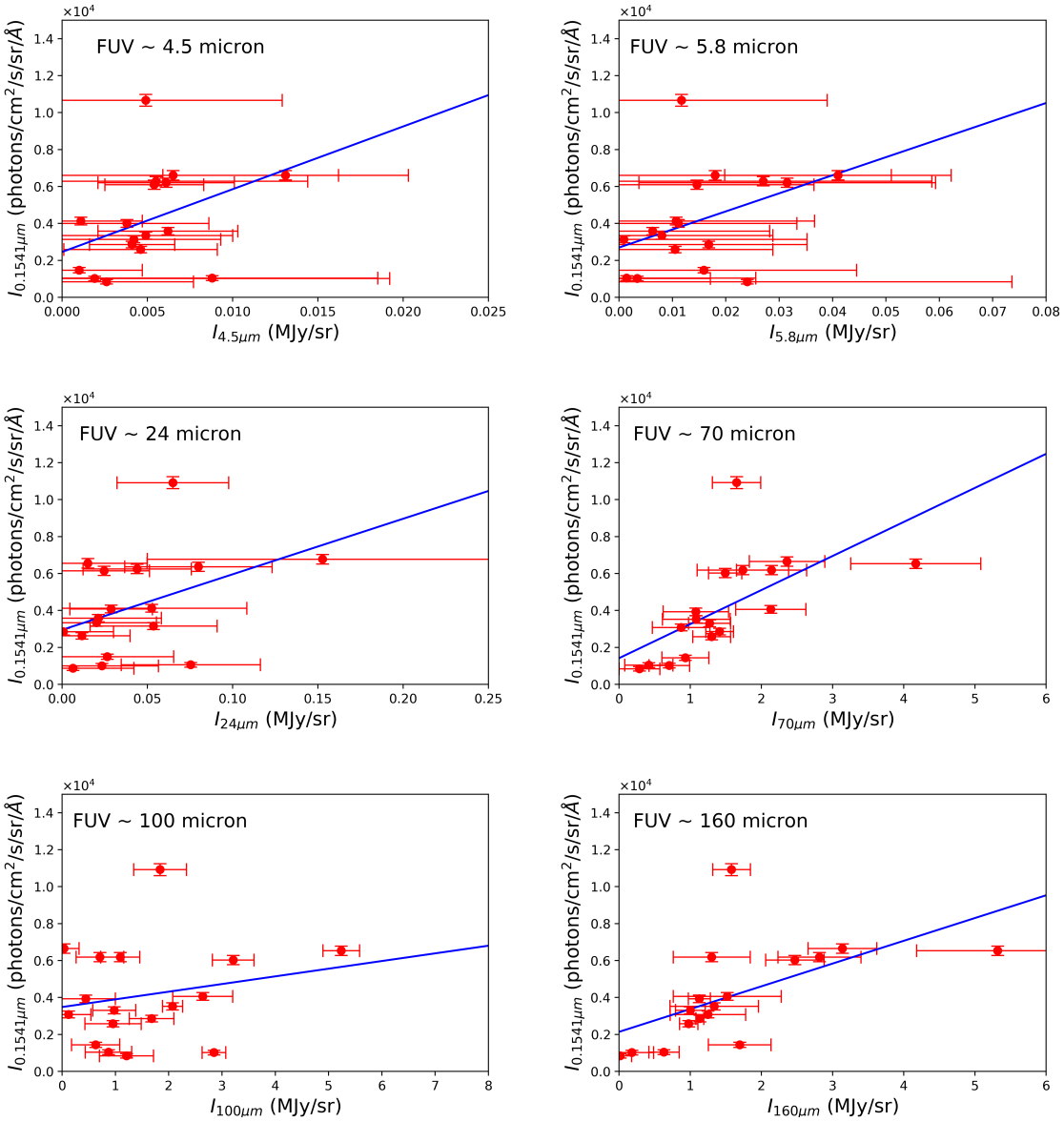

Fig. 4.1 FUV–IR correlation plots for 17 selected locations with N(HI) $> 1 \times 10^{21}$ cm $^{-2}$. The straight lines represent linear fits

size ratio of IR emitting clouds, because clouds with smaller radii and cross-sections absorb a smaller amount of the heating UV photons. Local variations in the dust-size distribution function cannot be excluded either, though they don't seem likely given that the areas under consideration are located far from high-density star formation regions with frequent SNe shocks harmful for dust. However, as we will see below in Table 4.3, the overall trend of the derivative dI_{ir}/dI_{uv} versus λ_{ir} indicates that UV heating is the primary cause that determines dust emission intensity along with its variations.

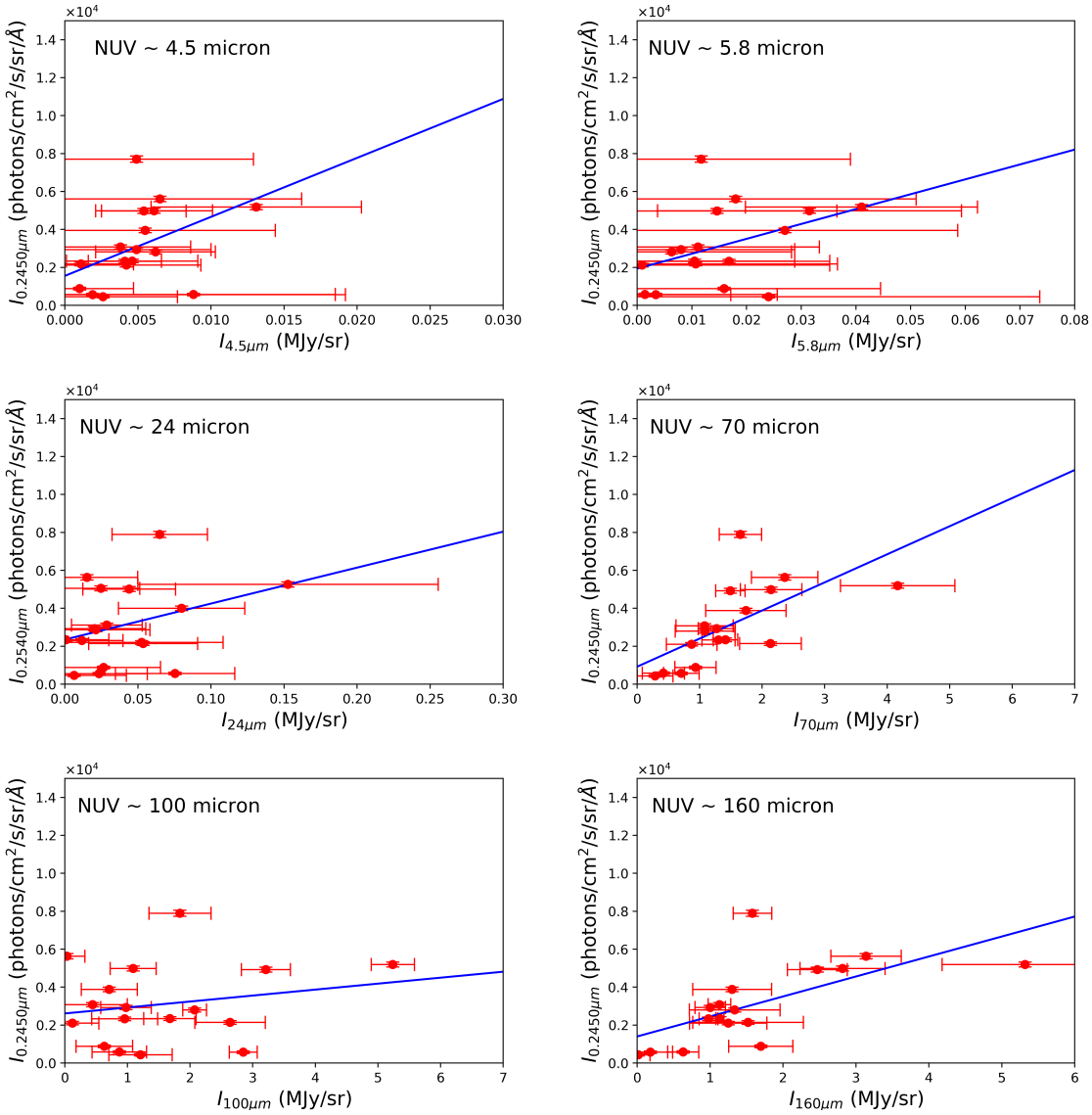

Fig. 4.2 NUV–IR correlation plots for 17 selected locations with N(HI) $> 1 \times 10^{21}$cm^{-2}. Straight lines represent linear fits

Table 4.3 Best-fit ratios of IR and UV intensities in units of 10^{-5} MJy/(phot/cm^2/s/Å) for locations with N(HI) $> 1 \times 10^{21}$ cm^{-2}

	$dI_{4.5}/dI_{uv}$	$dI_{5.8}/dI_{uv}$	dI_{24}/dI_{uv}	dI_{70}/dI_{uv}	dI_{100}/dI_{uv}	dI_{160}/dI_{uv}
FUV	0.29	1.02	3.32	54.2	240.9	81.1
NUV	0.32	1.27	5.27	67.5	318.1	94.9

We analyse the UV–IR correlations (both FUV–IR and NUV–IR) for our selected locations through the computation of Pearson and Spearman correlation coefficients. Our

findings indicate that the Pearson coefficient better represents our outcomes, indicating that the UV–IR correlation follows a linear relationship rather than a monotonic relationship.

Table 4.4 FUV–IR and NUV–IR correlation values for locations with N(HI) $> 1 \times 10^{21}$ cm^{-2} (Figs. 4.1 and 4.2)

FUV–IR	Pearson coefficient (r)	p-value	NUV–IR	Pearson coefficient (r)	p-value
FUV $\sim I_{4.5\mu m}$	0.14	0.13	NUV $\sim I_{4.5\mu m}$	0.17	0.07
FUV $\sim I_{5.8\mu m}$	0.17	0.10	NUV $\sim I_{5.8\mu m}$	0.16	0.09
FUV $\sim I_{24\mu m}$	0.28	0.09	NUV $\sim I_{24\mu m}$	0.21	0.18
FUV $\sim I_{70\mu m}$	0.57	0.007	NUV $\sim I_{70\mu m}$	0.59	0.005
FUV $\sim I_{100\mu m}$	0.19	0.42	NUV $\sim I_{100\mu m}$	0.19	0.44
FUV $\sim I_{160\mu m}$	0.54	0.01	NUV $\sim I_{160\mu m}$	0.61	0.005

Table 4.5 FUV–IR and NUV–IR correlation values for locations with N(HI) $< 1 \times 10^{21}$ cm^{-2} (Fig. 4.3)

FUV–IR	Pearson coefficient (r)	p-value	NUV–IR	Pearson coefficient (r)	p-value
FUV $\sim I_{4.5\mu m}$	0.06	0.10	NUV $\sim I_{4.5\mu m}$	0.05	0.17
FUV $\sim I_{5.8\mu m}$	0.18	0.07	NUV $\sim I_{5.8\mu m}$	0.17	0.08
FUV $\sim I_{24\mu m}$	-0.14	0.22	NUV $\sim I_{24\mu m}$	-0.14	0.29
FUV $\sim I_{70\mu m}$	0.07	0.77	NUV $\sim I_{70\mu m}$	0.23	0.29
FUV $\sim I_{100\mu m}$	-0.20	0.42	NUV $\sim I_{100\mu m}$	-0.25	0.32
FUV $\sim I_{160\mu m}$	0.37	0.08	NUV $\sim I_{160\mu m}$	0.51	0.01

Tables 4.4 and 4.5 present the observed Pearson correlation coefficients between FUV and IR data, as well as NUV and IR data for the two location groups. A comparison between the two tables reveals that in Table 4.4, a reasonably strong correlation emerges between the FUV and IR bands at 70 and 160 μm, demonstrating statistically significant coefficients. Notably, the highest correlation coefficients are observed at 70 μm compared to the other IR wavelengths. This outcome suggests that the MIR emission in Ho II predominantly stems from warm dust emission, in agreement with the MIR spectra typically observed in low-metallicity dwarf galaxies. Conversely, locations associated with low N(HI) predominantly exhibit a poor or even a weak negative correlation between the UV and IR intensities, except at 160 μm (see Table 4.5) which shows a reasonable correlation with NUV. This may imply either the presence of colder dust grains in cavities being irradiated by the general radiation field, or insufficient amount of dust. Furthermore, the p-values indicate that these correlations are statistically insignificant, as indicated in Table 4.5.

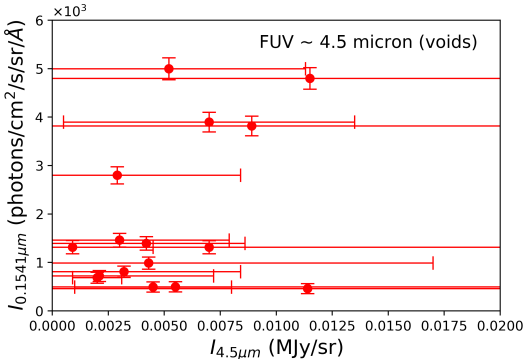
FUV ~ 4.5 micron (voids)
$I_{0.1541\mu m}$ (photons/cm^2/s/sr/Å)
$I_{4.5\mu m}$ (MJy/sr)

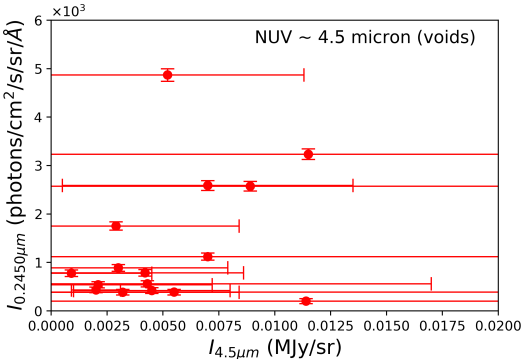
NUV ~ 4.5 micron (voids)
$I_{0.2450\mu m}$ (photons/cm^2/s/sr/Å)
$I_{4.5\mu m}$ (MJy/sr)

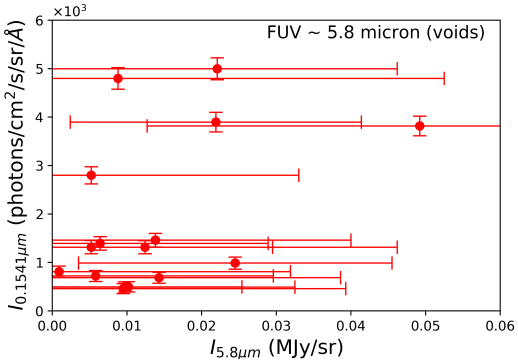
FUV ~ 5.8 micron (voids)
$I_{0.1541\mu m}$ (photons/cm^2/s/sr/Å)
$I_{5.8\mu m}$ (MJy/sr)

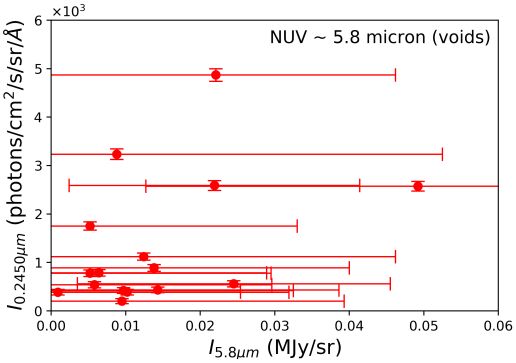
NUV ~ 5.8 micron (voids)
$I_{0.2450\mu m}$ (photons/cm^2/s/sr/Å)
$I_{5.8\mu m}$ (MJy/sr)

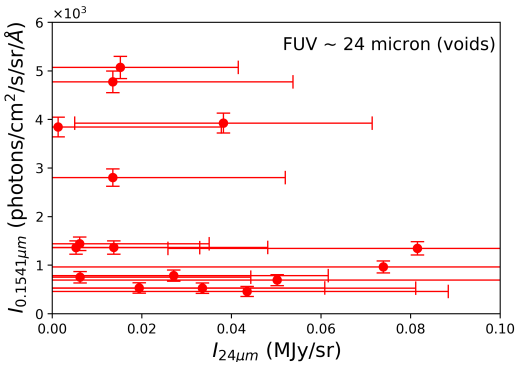
FUV ~ 24 micron (voids)
$I_{0.1541\mu m}$ (photons/cm^2/s/sr/Å)
$I_{24\mu m}$ (MJy/sr)

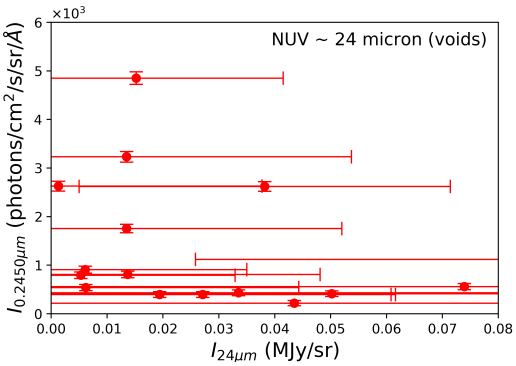
NUV ~ 24 micron (voids)
$I_{0.2450\mu m}$ (photons/cm^2/s/sr/Å)
$I_{24\mu m}$ (MJy/sr)

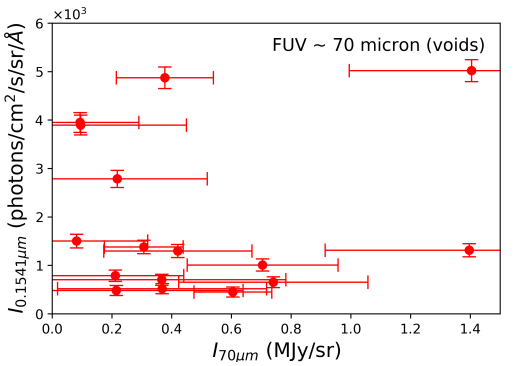
FUV ~ 70 micron (voids)
$I_{0.1541\mu m}$ (photons/cm^2/s/sr/Å)
$I_{70\mu m}$ (MJy/sr)

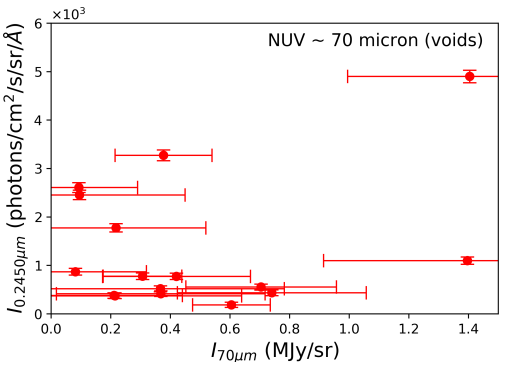
NUV ~ 70 micron (voids)
$I_{0.2450\mu m}$ (photons/cm^2/s/sr/Å)
$I_{70\mu m}$ (MJy/sr)

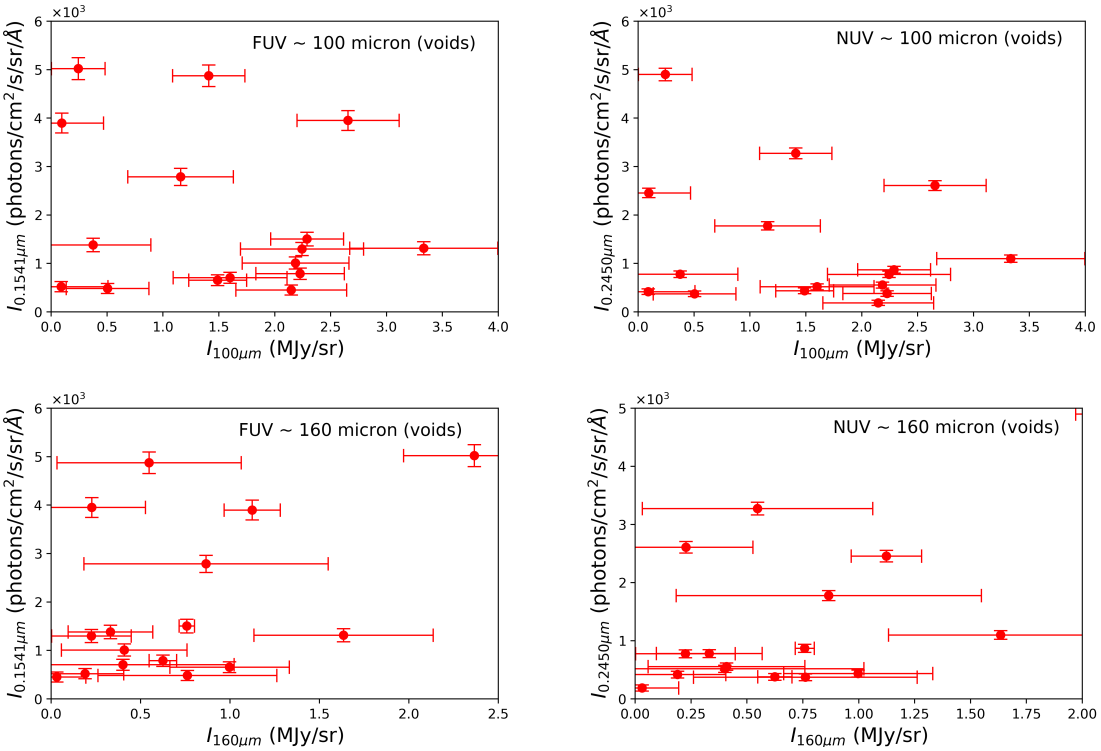

Fig. 4.3 FUV–IR and NUV–IR intensity plots for 16 locations with N(HI) $< 1 \times 10^{21}$ cm^{-2}

The MIR spectra of Ho II notably indicate a suppression of 8 μm emission attributed to PAH molecules within this galaxy (as discussed in [155]). Similarly, through our photometric measurements, we also observed the absence of 8 μm emission across all the locations we considered. Given this suppression in emission, we didn't calculate the correlation at 8 μm.

The interrelations between the FUV and IR, and between the NUV and IR flux densities are similar. Such a similarity can take place if the dominant source of dust heating is due to UV radiation, with the interrelation between FUV and NUV intensities being spatially invariant, indicating their common origin.

It is worth noting that the slopes of the correlations between the IR and UV intensities vary at different IR wavelengths as seen in Fig. 4.1: they increase from the shorter towards longer wavelengths, except at 160 μm (see Table 4.3). This trend is consistent with the expected one, if the dust heating is determined by diffuse UV: the derivative dI_{ir}/dI_{uv} at shorter wavelengths decreases approximately as $\nu^{4+\beta}\exp(-h\nu/kT_d)$, with β being the dust spectral index; it is assumed that dust temperature $T_d \propto I_{uv}^{1/(4+\beta)}$.

4.4 Diffuse FUV emission in Ho II: 3D radiative transfer modelling for dust scattering

One of the known sources of diffuse FUV emission is the scattering of starlight by dust grains in the ISM. To assess the extent of contribution from the scattering of starlight by dust grains in the ISM to the diffuse FUV emission, we conducted radiative transfer modeling in FUV for selected locations.

We have derived the diffuse UV intensities at 33 specific locations (refer to Table 4.1), as outlined in the preceding section. In Fig. 4.4 (*Right*), locations with an HI column density greater than 1×10^{21} cm^{-2} are denoted by purple circles, while locations featuring an HI column density below 1×10^{21} cm^{-2} (termed void locations) are marked by white squares. These diffuse intensities span a range of approximately 450-10000 photon units, with the brightest values typically associated with regions in proximity to star-forming regions. During radiative transfer modelling, the scattered intensity is quantified using two important wavelength-dependent parameters — the single scattering albedo α and the scattering phase function asymmetry parameter g.

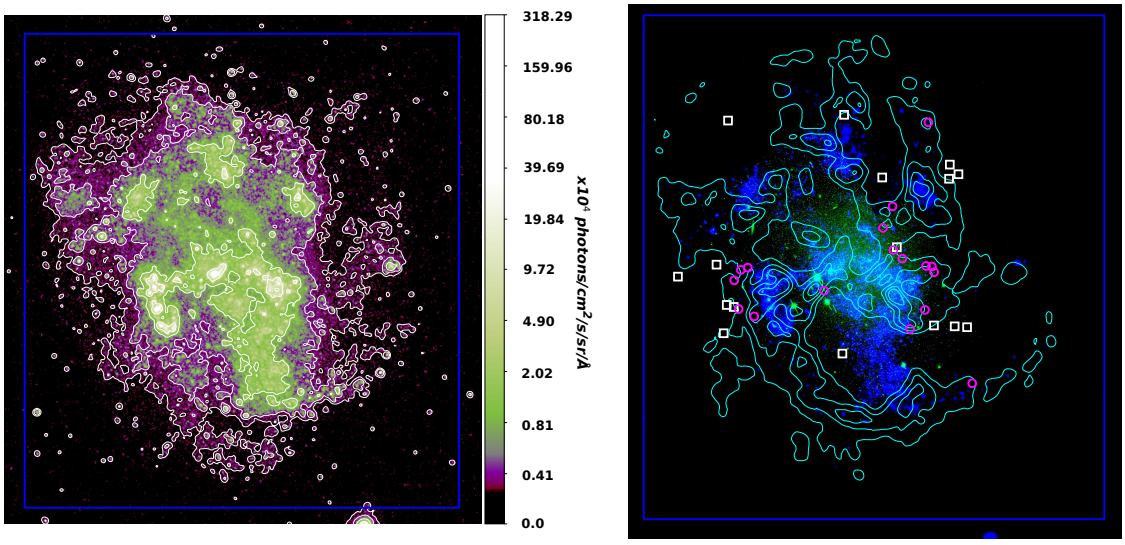

Fig. 4.4 *Left*: Smoothed FUV image of Ho II with isophotes overplotted for five intensity levels. *Right*: Multiband image of Ho II with FUV (F154W; *AstroSat*-UVIT) in blue, IR (3.6 μm; *Spitzer*) in green, and integrated HI map (THINGS) in teal contours. The HI contour corresponds to N(HI) = 1×10^{21} cm^{-2}. Selected diffuse UV locations with N(HI) $> 1 \times 10^{21}$ cm^{-2} are indicated by purple circles, and locations with N(HI) $< 1 \times 10^{21}$ cm^{-2} are indicated by white squares. It is evident from the figure that the locations with N(HI) $< 1 \times 10^{21}$ cm^{-2} mostly lie in the cavities devoid of HI gas

4.4.1 Single scattering model

To predict the dust scattered intensities in the FUV for Ho II, we employed a single-scattering radiative transfer model previously validated for the Orion region [95]. It involves a single interaction between photon and the dust particle or molecules, enabling straightforward calculations and efficient analysis of scattering behavior. Since Galactic UV diffuse emission has been known to originate mainly from the forward scattering by optically thin dust clouds in front of hot UV emitting stars [166], hence a single scattering model is considered for our study. This model effectively restricts the albedo α and the asymmetry factor g of the dust grains within the galaxy [95, 167]. Our adopted single-scattering model assumes dust distribution in a sheet in front of the UV emitting sources. However, it's important to note that in reality, scattering in Ho II might also involve back scattering from clouds situated behind the stars — a factor not addressed in this study. The intensity of scattered light depends on dust optical properties, including the albedo α, phase function $\phi(\theta)$, and optical depth values τ_1 and τ_2, as governed by the following equation:

$$I_{sca} = \frac{L_{star} \times \alpha \times \phi(\theta) \times \tau_1 \times e^{-\tau_2}}{4\pi d^2} \tag{4.4}$$

Here, τ_1 signifies the optical depth attributed to the scattering layer, expressed as $\tau_1 = n\sigma dz$, where σ denotes the extinction cross-section, n represents the dust number density, and dz stands for the layer's thickness. Meanwhile, τ_2 represents the optical depth of the residual material responsible for line-of-sight (LOS) extinction, whereby $\tau = \tau_1 + \tau_2$ denotes the overall optical depth at a specific location. Other parameters include the source luminosity L_{star}, and d signifies the distance between the source and the scattering layer.

The model employs the Henyey-Greenstein scattering phase function [168], expressed as:

$$\phi(\theta) = \frac{1 - g^2}{4\pi[1 + g^2 - 2g\cos(\theta)]^{3/2}} \tag{4.5}$$

where $\phi(\theta)$ denotes the energy scattered per unit solid angle in a given direction θ. The asymmetry factor g lies within the range of $[-1, 1]$. A value of g near to 0 implies isotropic scattering, a value close to -1 indicates strong backward scattering, while nearing 1 suggests strong forward scattering.

4.4.2 Sources of UV emission in Ho II

The primary sources of UV radiation within the galaxy are the star-forming complexes, extensively described in [108], each hosting multiple young star clusters. To determine the

observed fluxes of these clusters in the FUV, we referred to values specifically at $\lambda = 1521$ Å, from [121]. These values were initially corrected for galactic foreground extinction. To derive the intrinsic luminosity of these complexes, we additionally corrected for the internal extinction affecting these complexes based on their $E(B-V)$ values [121]. When computing the internal extinction within Ho II, [121] adopted an LMC reddening law due to the galaxy's similar metallicity and abundance [106, 169]. They presumed the metallicity of Ho II to be $Z = 0.4Z_{\odot}$.

Subsequently, utilizing these $E(B-V)$ values, we computed the optical depth τ, which enables us for the correction for interstellar absorption: $\tau = \frac{E(B-V)R_V}{1.0863}$. In this calculation, we utilized $R_V = 3.41$ to represent the average LMC reddening [170]. The flux densities are then multiplied with e^{τ} to accommodate the impact of internal extinction. Further, to compute the luminosities of these complexes, we assume the star clusters to reside at a distance of 3.39 Mpc, the estimated distance to the Ho II galaxy.

The total hydrogen column density $N(H)$ towards the complexes was calculated using the following relation for the LMC [11],

$$\frac{E(B-V)}{N(H)} = 4.5 \times 10^{-23}\,\mathrm{cm}^2/\mathrm{H} \tag{4.6}$$

Table 4.6 Properties of the contributing star-forming complexes. The complexes have been adopted from [108]

Complexes	Luminosity (erg s^{-1} Å^{-1})	N(H) (cm^{-2})
NE	6.28×10^{37}	1.27×10^{21}
N	11.15×10^{37}	1.62×10^{21}
NW	10.56×10^{37}	1.08×10^{21}
ExtN	5.49×10^{37}	1.77×10^{21}
SE	5.508×10^{37}	0.77×10^{21}
ExtNE	1.054×10^{37}	2.88×10^{21}
Int.shell	11.35×10^{37}	1.99×10^{21}

4.4.3 Results and Discussions

Given the unknown relative distribution and arrangement of stars and dust within Ho II, we have assumed that the scattering dust grains are distributed in the form of optically thin

filaments, situated at various distances between the observer and the star clusters for different locations. For computing the overall optical depth (τ) along the line of sight (LOS), we calculate the total $N(H)$ and multiply it by the extinction cross-section of dust, denoted as σ. When a location resides within the LOS of any of the star-forming complexes, we consider the $N(H)$ value pertaining to that complex, considering it as the $N(H)$ for the location, and subsequently multiplying it by σ to derive the optical depth. Conversely, if a location lies beyond the LOS of the star-forming complexes, we obtain the $N(H)$ value from the THINGS integrated HI map to compute the optical depth τ for that specific location. During the calculation of scattered intensity at each location, we account for the individual contribution from each star-forming complex separately, summing them to determine the total scattered intensity at that specific location. Our model provides scattered intensities for each combination of albedo α, asymmetry factor g, and scattering optical depth τ_1. By altering these parameters alongside the distance (d) between the star and the dust cloud, we can derive optimal optical constants and the 3D distribution of dust at diffuse locations. These best-fit parameter values are obtained through the minimization of the χ^2-statistic and considering a range of parameter values within a 90% confidence level.

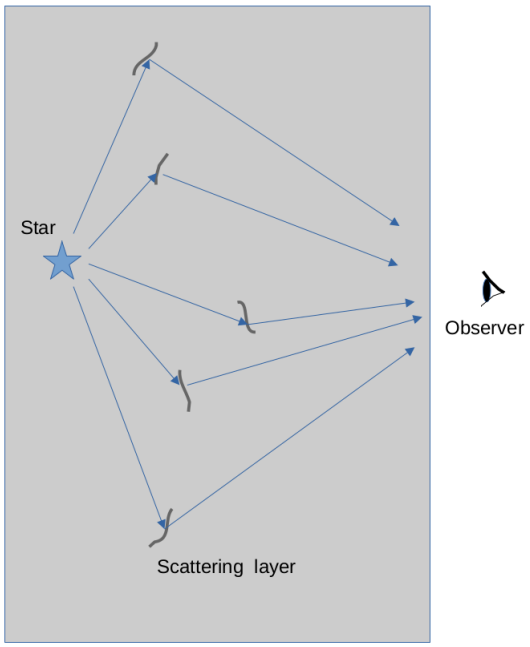

Fig. 4.5 Schematic diagram showing the relative geometry of the source (star) and the scattering of starlight by optically thin clouds towards the observer

Table 4.7 The values of the best-fit parameters (based on minimum χ^2-statistic) for locations with N(HI) > 1×10^{21} cm^{-2}. The range of values within 90% confidence level for each parameter are shown inside parentheses. The location numbers are in tally with Table 4.1

Locations	l (degrees)	b (degrees)	α	g	τ_1	τ_2	distance (pc)
1	144.2995	32.6691	0.3 (0.1-0.3)	0.6 (0.1-0.6)	0.041 (0.041-0.123)	0.369 (0.369-0.287)	140 (47-140)
3	144.2835	32.7029	0.4 (0.1-0.4)	0.3 (0.2-0.4)	0.122 (0.122-0.366)	1.098 (1.098-0.854)	93 (47-140)
6	144.2682	32.7303	0.4 (0.1-0.4)	0.4 (0.0-0.4)	0.041 (0.041-0.082)	0.369 (0.369-0.328)	140 (93-186)
9	144.3063	32.6755	0.2 (0.1-0.3)	0.4 (0.2-0.7)	0.124 (0.062-0.124)	0.496 (0.558-0.496)	47 (47-93)
10	144.2544	32.6734	0.1 (0.1-0.2)	0.4 (0.1-0.4)	0.088 (0.044-0.088)	0.352 (0.396-0.352)	140 (93-186)
14	144.2816	32.6657	0.1 (0.1-0.2)	0.5 (0.4-0.6)	0.060 (0.060-0.120)	0.540 (0.540-0.480)	140 (47-186)
15	144.2885	32.7289	0.2 (0.2-0.6)	0.6 (0.2-0.6)	0.058 (0.029-0.058)	0.232 (0.261-0.232)	140 (93-186)
16	144.2847	32.6633	0.2 (0.1-0.2)	0.5 (0.3-0.7)	0.062 (0.062-0.124)	0.558 (0.558-0.496)	140 (93-186)
19	144.2226	32.6552	0.1 (0.1-0.2)	0.5 (0.2-0.6)	0.046 (0.046-0.092)	0.414 (0.414-0.368)	186 (93-186)
21	144.3336	32.6575	0.2 (0.1-0.2)	0.5 (0.3-0.7)	0.082 (0.082-0.123)	0.328 (0.328-0.287)	186 (140-186)
22	144.2679	32.7278	0.3 (0.2-0.6)	0.5 (0.2-0.7)	0.049 (0.049-0.098)	0.441 (0.441-0.392)	93 (93-140)
23	144.2625	32.6781	0.1 (0.1-0.3)	0.7 (0.3-0.7)	0.041 (0.041-0.082)	0.369 (0.369-0.328)	93 (93-186)
25	144.2843	32.7338	0.1 (0.1-0.3)	0.4 (0.3-0.6)	0.049 (0.049-0.098)	0.441 (0.441-0.392)	140 (140-186)
26	144.2823	32.6637	0.1 (0.1-0.2)	0.5 (0.3-0.6)	0.124 (0.062-0.124)	0.496 (0.558-0.496)	140 (140-186)
30	144.2723	32.6760	0.3 (0.1-0.3)	0.4 (0.3-0.6)	0.062 (0.062-0.124)	0.558 (0.558-0.496)	93 (93-140)
32	144.2721	32.7334	0.5 (0.3-0.6)	0.2 (0.1-0.3)	0.029 (0.029-0.058)	0.261 (0.261-0.232)	140 (140-186)
33	144.2765	32.6735	0.2 (0.1-0.3)	0.6 (0.3-0.6)	0.046 (0.046-0.092)	0.414 (0.414-0.368)	93 (47-140)

For our dust scattered emission modeling, we specifically focused on locations where the HI column density exceeded 1×10^{21} cm^{-2}, as these regions exhibited detectable dust emissions. Our model relies chiefly on input parameters such as the luminosities of the star-forming complexes and the extinction cross-section σ. Given our assumption of an LMC reddening law, we considered the σ value corresponding to the LMC at our mean wavelength of 1541 Å. Subsequently, we compared our model-derived intensities with the FUV intensity values obtained from *AstroSat* to ascertain the most suitable values for α, g, and the distance to various dust locations. This comparison helped in determining the best-fitted parameters for our model.

Through our calculations, we have derived median values of $\alpha = 0.2$ and $g = 0.5$ at 1541 Å, for the dust grains present in Ho II. This finding aligns reasonably well with the theoretically predicted values of $\alpha = 0.3$ and $g = 0.6$ for an average LMC dust at a similar wavelength [171]. Our model-derived optical depths indicate an optically-thin scattering medium ($\tau \sim 0.02$ to 0.12) situated at distances ranging approximately from ∼47 pc to ∼186 pc ahead of the stars.

The slight deviation between observed and theoretical values might stem from uncertainties in the star-dust configuration and the use of the Henyey-Greenstein phase function at $\lambda < 0.16, \mu m$ [171]. While this phase function offers a good approximation to the calculated scattering phase function within wavelengths of $\sim 4, \mu m$ and $1, \mu m$, it fails to provide an

accurate fit at shorter wavelengths, notably in the UV spectrum. Considering Ho II's metallicity to be 0.1 $Z_{\odot}$ [99], its extinction law would resemble that of the SMC. Consequently, the extinction cross-section σ would decrease by roughly a factor of $\sim$3 due to the SMC's dust-to-gas ratio being approximately one-third of the LMC's [172]. This alteration would require a nearly threefold increase in the dust grains' albedo in the model, a value significantly higher than the theoretical predictions for the Magellanic clouds.

Table 4.7 demonstrates that the optical depths (τ_1) of the scattering layer are minimal, with a median value of 0.061, compared to the optical depths of the layer responsible for LOS extinction. This suggests forward scattering by optically thin clouds, resembling observations within our own galaxy [166].

4.5 Diffuse IR emission in Ho II: Multi-temperature dust populations

For local dwarf galaxies to yield pertinent insights into understanding their more distant counterparts, conducting a comparative assessment of their overall emission traits, on a smaller scale, holds prominent significance [1, 173]. The *Spitzer* and *Herschel* space telescopes, with an angular resolution of $\sim 2'' - 5''$, offer meticulous scrutiny of Ho II's interstellar disc. Employing this level of resolution in surveying the ISM holds the potential to differentiate isolated star-forming regions, photodissociation regions, H II regions, supernova remnants, and provides the insights into relevant physical processes. This study focuses on the analysis of IR spectra emanating from dust emissions spanning the range of $\lambda = 4.5, , \ldots 160 \mu$m, extracted from archival data obtained by *Spitzer* and *Herschel*, concentrating on a select few relatively small-area locations.

Given that the primary mechanism for dust heating involves the absorption of UV/optical photons, we have incorporated the highest resolution UVIT FUV observations of the Ho II galaxy. These observations play a pivotal role in comprehending the UV radiation fields, which influence the alteration of dust populations and shape their thermal IR emission profiles at these specific locations.

4.5.1 Observational data

The process of observing and subsequently correcting the IR data for stellar contamination has been previously described in Sec. 4.3.1. In this particular study, we chose 50 random

locations across the galaxy, spanning areas within the star-forming regions, their peripheries, and even the HI voids. In alignment with the suggested scarcity of PAH in this galaxy [77], a majority of these regions exhibited an absence of 8 μm emission, except three specific locations. These 8 μm emissions are exclusively detected in H II regions [156]. Following this, locations without detectable IR emission across all the considered wavelengths were excluded, resulting in a final set of 27 locations. The IR intensities for these finalized locations, extracted within $5''$-radius circular apertures along with their respective errors, are presented in Table 4.8. Additionally, they are plotted on the FUV image captured on December 9, 2016, shown in Fig. 4.6.

Table 4.8 IR intensities in selected 27 locations. Colour coding is according to Fig. 4.6. See Sec. 4.3.1 for details of calculations

Location No	l (degrees)	b (degrees)	$I_{4.5\mu m}$ (MJy sr^{-1})	$I_{5.8\mu m}$ (MJy sr^{-1})	$I_{8\mu m}$ (MJy sr^{-1})	$I_{24\mu m}$ (MJy sr^{-1})	$I_{70\mu m}$ (MJy sr^{-1})	$I_{100\mu m}$ (MJy sr^{-1})	$I_{160\mu m}$ (MJy sr^{-1})
1	144.2731	32.6844	0.0106 ± 0.0273	0.0330 ± 0.0158	0 ± 0.0141	0.0333 ± 0.0100	1.9079 ± 0.0742	0.2300 ± 0.526	3.5553 ± 0.3761
2	144.2898	32.6750	0.0069 ± 0.0075	0.0200 ± 0.0079	0 ± 0.0062	0.1092 ± 0.0121	5.2336 ± 0.4443	7.2000 ± 0.5544	3.8332 ± 0.4575
3	144.2512	32.6607	0.0055 ± 0.0015	0.0122 ± 0.0035	0 ± 0.0065	0.6279 ± 0.1453	7.7358 ± 1.2877	14.4400 ± 2.5546	1.6263 ± 0.5952
4	144.2952	32.7203	0.0114 ± 0.0016	0.0191 ± 0.0035	0 ± 0.0043	0.3012 ± 0.0467	5.9099 ± 0.1316	8.7800 ± 0.8157	3.7606 ± 0.1606
5	144.2699	32.6985	0.0098 ± 0.0068	0.0340 ± 0.0064	0 ± 0.0053	0.1225 ± 0.0153	4.5948 ± 0.4802	1.9600 ± 0.4780	4.5118 ± 0.3977
6	144.2882	32.6942	0.0112 ± 0.0038	0.0245 ± 0.0037	0 ± 0.0045	0.0694 ± 0.0077	1.8620 ± 0.1317	2.4400 ± 0.4311	2.8699 ± 0.0896
7	144.2960	32.6858	0.0053 ± 0.0023	0.0171 ± 0.0040	0 ± 0.0041	0.0376 ± 0.0119	2.3811 ± 0.1101	3.8800 ± 0.3801	3.0756 ± 0.2645
8	144.2816	32.6822	0.0183 ± 0.0218	0.0619 ± 0.0147	0.0393 ± 0.0217	0.3235 ± 0.0269	5.0719 ± 0.3350	10.6100 ± 0.4589	5.0871 ± 0.0997
11	144.2757	32.6922	0.0094 ± 0.0045	0.0361 ± 0.0043	0 ± 0.0040	0.1135 ± 0.0067	4.9482 ± 0.3170	4.1600 ± 0.7900	1.8229 ± 0.7535
12	144.2774	32.6973	0.0527 ± 0.0132	0.0809 ± 0.0320	0.1682 ± 0.0759	1.8455 ± 0.2469	14.7611 ± 1.0000	22.1000 ± 1.2138	5.3792 ± 0.3122
19	144.2630	32.6846	0.0103 ± 0.0077	0.0261 ± 0.0073	0 ± 0.0054	0.1034 ± 0.0222	1.9352 ± 0.1041	1.2400 ± 0.4014	3.6667 ± 0.4822
21	144.2754	32.7183	0.0115 ± 0.0082	0.0327 ± 0.0056	0 ± 0.0059	0.5014 ± 0.1046	9.3478 ± 0.7582	10.7500 ± 0.3933	5.1692 ± 0.1822
24	144.2618	32.7021	0.0150 ± 0.0328	0.0467 ± 0.0212	0 ± 0.0142	0.1520 ± 0.0269	3.0249 ± 0.2186	3.8500 ± 0.6202	3.1424 ± 0.8492
27	144.3054	32.6733	0.0004 ± 0.0608	0.0216 ± 0.0361	0 ± 0.0205	0.0246 ± 0.0077	1.6464 ± 0.0832	3.5500 ± 0.4701	1.9316 ± 0.1883
30	144.2863	32.7213	0.0204 ± 0.0054	0.0278 ± 0.0070	0 ± 0.0089	0.7002 ± 0.0429	8.0550 ± 0.3701	10.9100 ± 0.4139	2.9251 ± 0.2354
32	144.2768	32.6716	0.0075 ± 0.0048	0.0249 ± 0.0049	0 ± 0.0048	0.0328 ± 0.0076	1.7242 ± 0.2066	0.5300 ± 0.4317	2.0164 ± 0.3426
33	144.2595	32.6931	0.0089 ± 0.0061	0.0408 ± 0.0052	0 ± 0.0058	0.0184 ± 0.0074	1.4919 ± 0.1011	0.8100 ± 0.3886	1.9019 ± 0.1035
35	144.2949	32.6935	0.0074 ± 0.0039	0.0372 ± 0.0062	0 ± 0.0045	0.0258 ± 0.0092	1.2994 ± 0.2115	0.3400 ± 0.4879	2.8701 ± 0.4514
36	144.3222	32.6821	0.0053 ± 0.0047	0.0048 ± 0.0046	0 ± 0.0040	0.0269 ± 0.0070	0.3790 ± 0.1105	0.4800 ± 0.3691	0.9162 ± 0.2116
37	144.2812	32.7059	0.0283 ± 0.0248	0.0783 ± 0.0157	0.0355 ± 0.0161	0.4197 ± 0.0166	4.7531 ± 0.1707	8.4700 ± 0.6406	5.6591 ± 0.2748
41	144.2905	32.7123	0.0065 ± 0.0032	0.0361 ± 0.0038	0 ± 0.0043	0.1141 ± 0.0109	3.0536 ± 0.3157	2.2200 ± 0.3941	2.5669 ± 0.1019
42	144.2438	32.6674	0.0029 ± 0.0022	0.0021 ± 0.0040	0 ± 0.0049	0.0256 ± 0.0064	1.2904 ± 0.1688	0.4700 ± 0.3980	1.2432 ± 0.3501
44	144.2809	32.6760	0.0077 ± 0.0293	0.0298 ± 0.0188	0 ± 0.0131	0.2634 ± 0.0461	4.4406 ± 0.3565	6.1000 ± 0.7717	3.7378 ± 0.2591
46	144.2714	32.7231	0.0089 ± 0.0050	0.0255 ± 0.0110	0 ± 0.0166	1.5858 ± 0.5204	8.9976 ± 1.1983	7.2400 ± 1.3546	3.6638 ± 0.4835
47	144.2778	32.7236	0.0231 ± 0.0045	0.0313 ± 0.0060	0 ± 0.0053	0.7442 ± 0.0395	9.7106 ± 0.5049	14.3700 ± 0.7789	5.2882 ± 0.1123
49	144.2435	32.7246	0.0119 ± 0.0831	0.0426 ± 0.0484	0 ± 0.0268	0.2938 ± 0.0202	1.8468 ± 0.1020	2.6500 ± 0.3166	1.7170 ± 0.0706
50	144.2854	32.6877	0.0039 ± 0.0026	0.0221 ± 0.0039	0 ± 0.0039	0.0306 ± 0.0075	3.2687 ± 0.3817	2.9900 ± 0.4238	3.0087 ± 0.4635

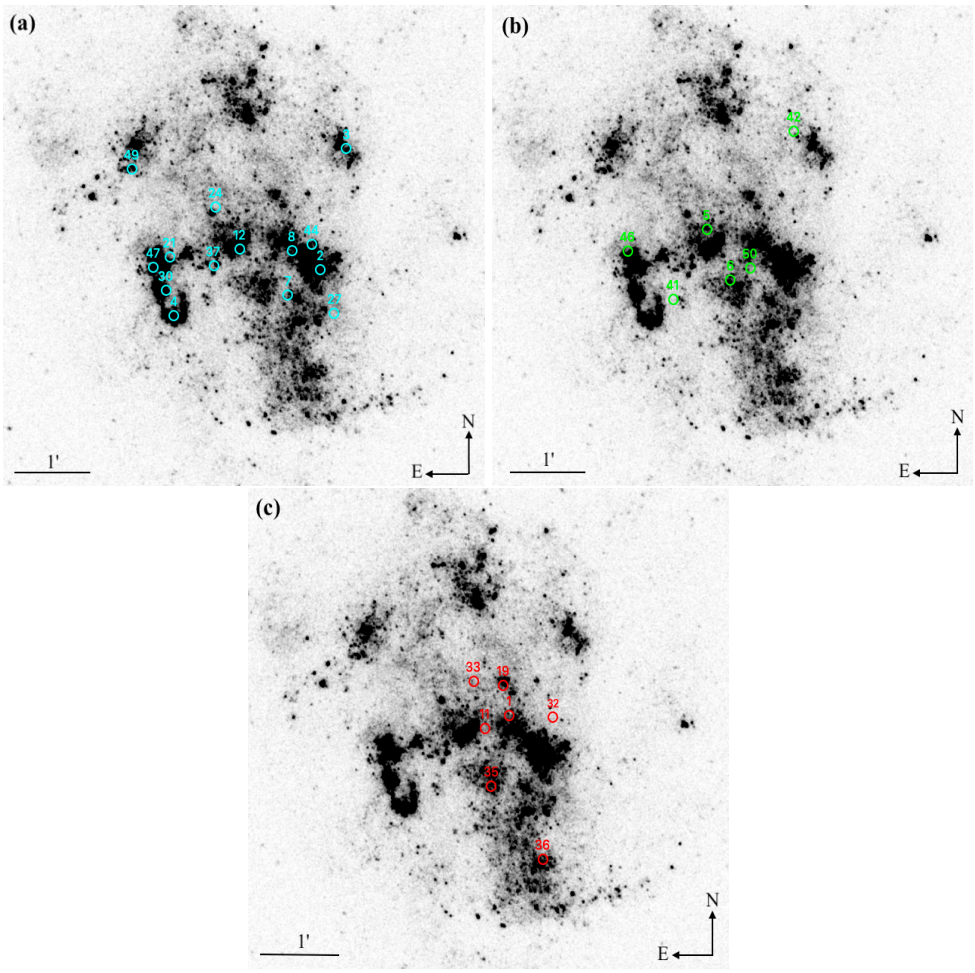

Fig. 4.6 Locations depicted in Table 4.8 overplotted on the FUV image of Ho II obtained by the UVIT instrument [114]. (a) Locations where intensity peaks at 100 μm, represented by cyan colour, mostly lie in the SFR, (b) Locations where intensity peaks at 70 μm, represented by green colour, lie mostly in the outskirts of SFR, (c) Locations lying in HI voids (N(HI) < 1×10^{21} cm^{-2}), represented by red colour. The circles representing the locations are of the same size as circular apertures ($5''$ radius) used to extract the IR intensities from the locations. The FUV image was taken on December 9, 2016 with an exposure time of around 9 ks

4.5.2 Analysis of IR dust emission

The locations detailed in Table 4.8 and depicted in Fig. 4.6 can be broadly categorized as follows:

1. Locations exhibiting a peak intensity approximately at 100 μm. Following this peak, these locations display a decreasing trend in intensities as the wavelengths extend beyond 100 μm.

2. Locations demonstrating a peak intensity around 70 μm. Subsequent to reaching this peak, the intensities generally decline toward 100 μm, followed by an increase towards 160 μm.

3. Locations corresponding to HI voids, defined as regions where the neutral hydrogen column density N(HI) is less than 1×10^{21} cm^{-2} [155]. These locations typically peak at 70 μm and exhibit a dip in intensity at 100 μm.

4. Locations with an additional emission specifically at 8 μm. These locations showcase intensity peaks around 100 μm, subsequently declining as wavelengths extend, mirroring the trend observed in category (i) locations.

4.5.3 Multi-temperature dust spectra

In our study, we attribute the variations observed in the aforementioned locations to contributions from multi-temperature dust components originating in different but sometimes unresolved regions within the same field of view.

The observed flux density from a dust cloud with a total mass M_d at a frequency ν is given by [174],

$$F_\nu = \frac{3M_d}{4\pi a \rho_d D^2} Q(a,\nu) B_\nu(T) \tag{4.7}$$

where a stands for the dust grain radius ($a \sim 0.1$ μm), ρ_d represents the density of the dust material, $B_\nu(T)$ denotes the Planck function, and D signifies the detector-cloud separation. Here, $Q(a,\nu) \simeq 0.01a(\nu/c)^\alpha$ represents the emissivity, with a and ν in cgs units. [175] consider a spectral index $\alpha = 1.94$, although a broader range of $\alpha = 1.5-2$ is commonly utilized [176, 177]. For the sake of simplifying the fitting process and accounting for observational uncertainties, we assume $\alpha = 2$ unless explicitly stated otherwise.

Fig. 4.7 displays IR spectra from four specific locations, one from each category outlined above, within the Ho II galaxy. To analyze these spectra, we employ a fitting procedure within the error margins, focusing on the dust temperature T_d and dust mass M_d, assuming a fixed spectral index $\beta = 2$. The dust mass M_d is reduced to the surface dust mass within the corresponding aperture defined by solid angle $\Delta\Omega$. Consequently, the fitting results yield the dust temperature T_d, the dust mass M_d for warm and hot ($T_d > 30$ K) compact dusty structures, and the surface dust mass Σ_d for colder ($T_d < 30$ K) dust likely distributed within

the diffuse ISM.

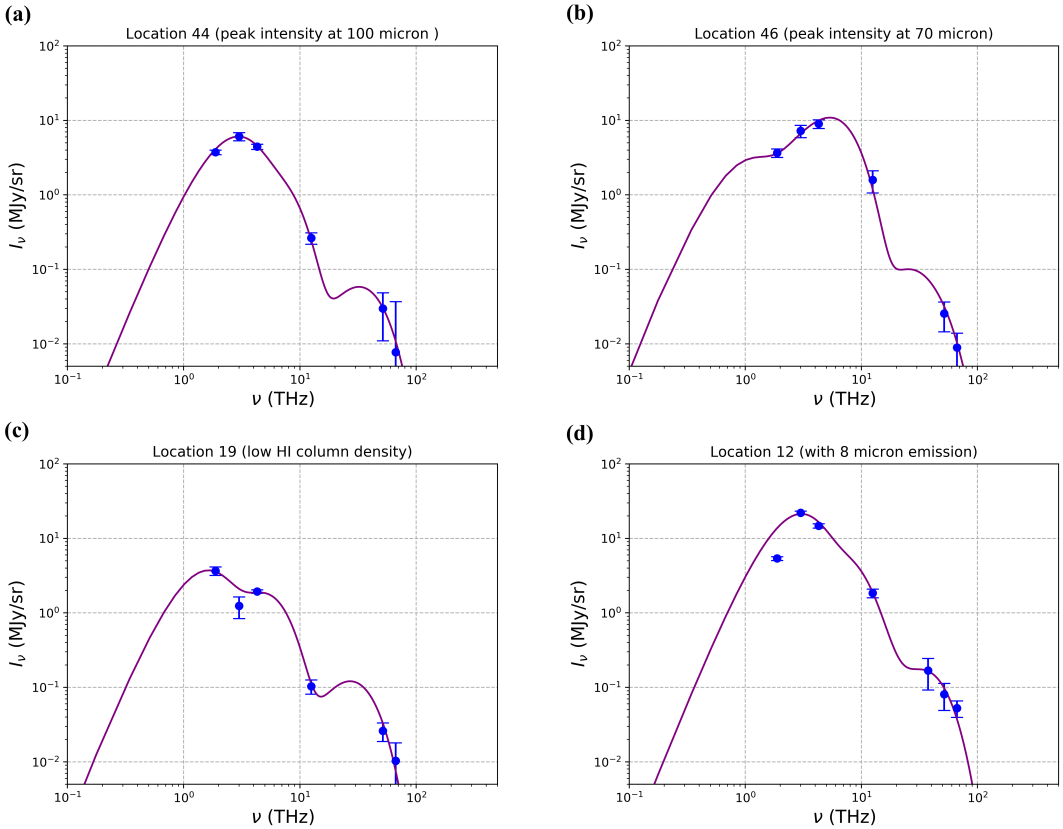

Fig. 4.7 Fits of the spectra of dust at different environmental conditions as classified in Fig. 4.6. They represent spectra of dust: **i)** spectra peaking at 100 μm, **ii)** spectra peaking at 70 μm, **iii)** in regions with HI column densities below the detection limit $N(\mathrm{HI}) < 10^{21}$ cm^{-2}, **iv)** spectra with emission at 8 μm, **v**) spectra with a weak intensity dip at 100 μm and **vi**) spectra with a strong intensity dip at 100 μm. Specifically, the presented spectra fitted with multi-temperature modified black body with the following temperatures and dust surface mass densities for cold components and dust masses for warm and hot ones: (a) $T = 27, 56, 310$ K ($\Sigma_d = 6 \times 10^{-5}\ M_\odot \mathrm{pc}^{-2}$, $M_d = 0.009,\ 6.4 \times 10^{-8} M_\odot$); (b) $T = 10, 25, 53, 220, 320$ K ($\Sigma_d = 3 \times 10^{-3} M_\odot \mathrm{pc}^{-2}$, $M_d = 0.5,\ 0.08,\ 4 \times 10^{-7},\ 4 \times 10^{-8}\ M_\odot$); (c) $T = 15, 46, 260$ K ($\Sigma_d = 7 \times 10^{-4}\ M_\odot \mathrm{pc}^{-2}$, $M_d = 0.025,\ 3 \times 10^{-7}\ M_\odot$); (d) $T = 28, 63, 100, 320$ K ($\Sigma_d = 6 \times 10^{-4}\ M_\odot \mathrm{pc}^{-2}$, $M_d = 63,\ 0.002,\ 2 \times 10^{-7}\ M_\odot$)

Preliminary assessments suggest the following: *(i)* Cold Dust at $T_d \simeq 10 - 30$ K likely originates from the diffuse ISM with a dust-to-gas mass fraction, $\zeta_d = (2 - 3) \times 10^{-3}$. These estimates are consistent with a lower metallicity assumption and suggest a gas scale height of $z_0 = 200$ pc and a plane gas density of $n = 1$ cm^{-3}. *ii)* dust at 30 to 50 K appears to stem from the ISM surrounding individual stars in close proximity. The average

surface dust mass density for the colder components ($T_d < 30$ K) is approximately $\langle \Sigma_d \rangle \sim (1-3) \times 10^{-3} M_\odot$ pc^{-2}. This suggests a total dust mass within a 1.5′ diameter of Ho II, around $\sim(1-30) \times 10^4\ M_\odot$, consistent with findings by [155]. The 'high-temperature' peaks with $T_d > 220$ K likely require alternative energy sources. These could include IR emission from dusty envelopes around red giants [178, 179], circumstellar discs [180], as well as dusty clumps in wind-blown bubbles and supernova remnants. The possibility of heating by stellar UV/FUV photons seems improbable due to the extremely high energy density required ($\nu u_\nu \sim 10^7$ times the Habing value $\nu u_{\nu,0} = 4 \times 10^{-14}$ erg cm^{-3}), as discussed in Section 12.5 of [181].

4.5.4 Results and Discussions

Analyzing dust thermal emissions on smaller spatial scales offers an advantage by avoiding the blurring effects of larger area averaging and the confusion arising from mixing different source characteristics. The *Spitzer* and *Herschel* space telescopes offer high-resolution observations of the nearby dwarf galaxy Ho II, benefiting from its relatively low inclination. This orientation enables the identification of contributions from smaller-scale features without significant mixing which can originate in crowded environments along sightlines. This method, once fully explored, holds promise as a valuable tool for identifying diverse dust populations in other nearby galaxies where achieving high spatial resolution is feasible, such as M31, LMC, SMC, and other dwarf galaxies within the Local Group.

In this work, among the infrared spectra acquired at diverse locations within the Ho II galaxy (refer to Fig. 4.7 and the caption for a brief overview), distinctive cloud like structures with notably varied spectra were identified. These spectral differences did not directly correlate with the three previously classified groups of sources highlighted in Fig. 4.6. For instance, the IR spectra within HI voids exhibited no obvious distinct features. Conversely, in compact regions close to the FUV-bright spots, likely associated with active star formation (even if not always directly linked to bright Hα regions observed by the *HST*), we observed three distinct categories of cloud-like structures showcasing apparently different temperature components - cold, warm, and hot. For the sake of simplicity, we attributed these distinctions to varying temperatures, within the simplest assumptions. We overlooked the contribution from PAH molecules, primarily due to their susceptibility to destruction under intense FUV radiation [155] (for recent discussions, see [182]).

It appears natural for the assumption that the coldest dust components are diffusely scattered throughout the ISM and heated by the FUV radiation field. Surprisingly, upon

preliminary examination, there seems to be no evident correlation between the temperatures of the cold dust components and the FUV radiation field for most of the locations (refer to Fig. 4.8). The temperatures observed for the cold dust components within HI voids and in locations with spectra peaking at 70 μm fall within the range of $10-20$ K, showing no apparent correlation with the FUV intensity. However, in the locations where the intensity peaks at 100 μm, slightly higher temperatures of approximately $20-30$ K are observed, seemingly increasing with the FUV intensity.

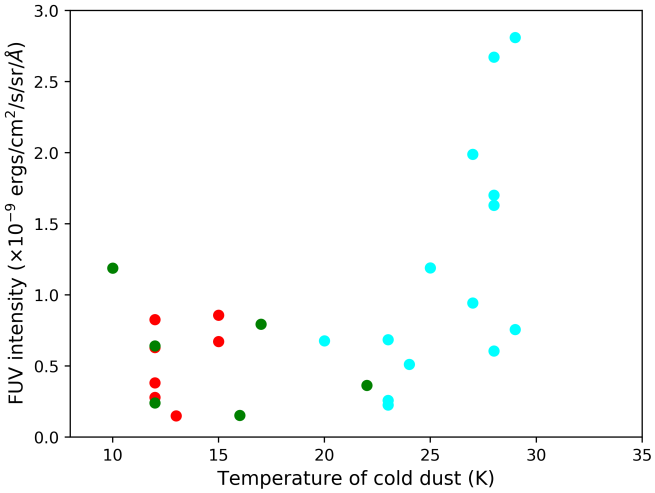

Fig. 4.8 Variation of temperature of cold dust with FUV intensity for the considered 27 locations. Colour coding is according to Fig. 4.6

It's noteworthy that in the refined spectra where the flux at 8 μm is notably above the detection threshold (locations 8, 12, 37 in Table 4.8), we have observed enhanced intensity in wavelengths near those typically associated with PAH features, at ~ 3.3 μm, ~ 6 μm, and ~ 24 μm. It's interesting to highlight that emissions within this range commonly stem from photodissociation regions, primarily due to the primary H_2 rotational lines spanning $\lambda = 6.9,,\ldots 17.0$ μm [183]. However, our investigation of Ho II hasn't revealed any previously reported detection or study of these features in the literature. Since the last available data up to 2010, no information on these spectral features in this wavelength range for Ho II is known. Consequently, under the aforementioned assumptions and guided by the arguments presented by [155] & [182], we have approximated the spectra in this wavelength range using a modified black body from sources characterized by higher temperatures. These sources are assumed to stem from compact energy sources like dusty envelopes surrounding red giant

stars, which might include carbon stars, along with dusty clumps heated by shock waves from stellar winds or SNe.

4.6 Conclusions

In this chapter, our focus was on investigating the ISM of the dwarf galaxy Ho II. We utilized UV observations from *AstroSat*/UVIT complemented with IR observations from *Spitzer*, and *Herschel* space telescopes to delve into the ISM's interstellar dust component. Specifically, in Sec. 4.3, we explored the relationship between diffuse UV and IR emissions within the galaxy through a correlation study. We found a stronger correlation between 70 μm IR emission and UV in regions with high HI density, suggesting that UV photons absorbed by warm dust near hot, young stars gets re-radiated. Interestingly, voids displayed poor or weak negative UV-IR correlation, except for 160 μm which showed a reasonable correlation with NUV, implying the presence of colder dust grains being irradiated by general radiation field or insufficient amount of dust. Moving to Sec. 4.4, our focus shifted to modeling diffuse FUV emission within the galaxy to explore the role of dust scattering in contributing to diffuse UV emission. Our model derived dust optical parameters showed reasonable agreement with theoretical predictions. This led us to conclude that the diffuse FUV emission in regions with high HI density includes a component of dust scattering. Notably, we identified a low optical depth for the layer responsible for scattering and a high g value, similar to earlier findings for our galaxy, suggesting forward scattering by optically thin clouds. However, assessments based on low albedo values and optical depths from our model suggested that only a small portion of the total diffuse FUV emission could originate from dust scattering. Lastly, in Sec. 4.5, we presented a first time analysis of IR dust emission in galaxy Ho II, aiming to identify spatial variations in dust parameters across small scales of $\sim$ 82 pc (equivalent to a circular area of 5$''$ radius). Our analysis unveiled spectra representing multiple dust populations — up to five, in locations connected to physically distinct regions, revealing different temperatures among these populations.